RSC Advances

PAPER

View Article Online
View Journal | View Issue

Cite this: *RSC Adv.*, 2023, **13**, 10036

Investigation of structural, morphological, and electrical conductivity study for understanding transport mechanisms of perovskite $CH_3NH_3HgCl_3$

Imen Gharbi, [a] Abderrazek Oueslati, *[a] Ayten Ates,[d] Abdelfattah Mahmoud, [b] Mustapha Zaghrioui[c] and Mohamed Gargouri[a]

Along with morphological and structural studies, the temperature and frequency dependence of the electrical and dielectric properties of the $CH_3NH_3HgCl_3$ (MATM) compound was investigated and analyzed. SEM/EDS and XRPD analyses proved the purity, composition, and perovskite structure of the MATM. DSC analysis reveals the existence of an order–disorder phase transition of a first-order type at about 342 ± 2 K and 320 ± 1 K (heating and cooling, respectively), attributed to the disorder of $[CH_3NH_3]^+$ ions. The overall results of the electrical study provide arguments for the ferroelectric nature of this compound and aim to broaden the current knowledge on the thermally activated conduction mechanisms of the studied compound *via* impedance spectroscopy. The electrical investigations have shown the dominant transport mechanisms in different frequency and temperature ranges, proposing the CBH model in the ferroelectric phase and the NSPT model in the paraelectric phase. The temperature dependence of the dielectric study reveals the classic ferroelectric nature of the MATM. As for the frequency dependence, it correlates the frequency-dispersive dielectric spectra with the conduction mechanisms and their relaxation processes.

Received 31st January 2023
Accepted 24th March 2023

DOI: 10.1039/d3ra00671a

rsc.li/rsc-advances

1. Introduction

To meet the continuous demands of industrial needs, new functional materials with tunable properties were created primarily in organic–inorganic hybrids.[1] These compounds present an emerging class of innovative and advanced new materials that hold significant promises.[2] Their complex structure, based on a molecular-scale composite of organic and inorganic components, allows the combination of the properties of these two classes of materials to obtain a unique material. Organic compounds are mainly characterized by weak interactions, namely van der Waals and hydrogen bonding. They have high luminescence efficiency potential, polarizability, plastic mechanical properties, and conductive behavior in some cases.[3] Inorganic compounds, typically characterized by covalent and ionic interactions, are known for their thermal stability and interesting properties such as electronic (high electrical mobility and wide range of band gap), magnetic, and dielectric properties.[3]

In the early 21st century (precisely in 2009 by Kojima *et al.*[4]), the use of perovskite belonging to the hybrid organic–inorganic materials with the AMX_3 (A = methylammonium, formamidinium, aziridinium, and methylhydrazinium,[5–7] M = lead and tin, and X = Cl, Br, I)[4–17] formula, in solar cells, leading the way in the photovoltaic industry.

They have become the domineering type of perovskites in the field of photovoltaics. In just a few years, the power conversion efficiency in solar cells, given by hybrid organic–inorganic perovskites, has rapidly increased by three times the initially promising value (9%).[8] In addition to their outstanding performance, their simple and cost-effective fabrication, *i.e.*, solution-processing techniques, make them one of the most desirable and most studied semiconductor materials in the photovoltaics field.[9] Other than their application in the field of photovoltaics, these compounds have been widely used in lasers, light-emitting diodes, photodetectors, and thermoelectricity.[10–14] Their extraordinary properties, including a direct bandgap, high carrier mobilities, a long lifetime of the carriers, low carrier recombination rates, long-range charge transport with low trap densities, efficient charge collection at the contacts, a high absorption factor, and a tunable spectral absorption range, are attributed to the unique electronic properties of these materials.[9,16] Thanks to the scientific community's enormous interest, the hybrid organic–inorganic

[a]*Laboratory of Spectroscopic Characterization and Optical Materials, Faculty of Sciences, University of Sfax, B.P. 1171, 3000 Sfax, Tunisia. E-mail: oueslatiabderrazek@yahoo.fr*

[b]*GREENMAT, CESAM, Institute of Chemistry B6, University of Liège, Liège 4000, Belgium*

[c]*Université François-Rabelais de Tours, Laboratoire GREMAN UMR-CNRS 7347, 15 rue de la Chocolaterie, IUT de Blois, 41029 Blois Cedex, France*

[d]*Department of Chemical Engineering, Engineering Faculty, Sivas Cumhuriyet University, 58140 Sivas, Turkey*

perovskites have quickly expanded in terms of types of materials by substituting one or more of the organic or inorganic ions in one of the most studied perovskites. Despite recent rapid advances in conversion efficiency, the understanding of the fundamental properties of AMX_3 perovskites remains limited.

The "Methylammonium Trichloro-Mercurate CH_3NH_3-$HgCl_3$" (MATM) belonging to the perovskite-type AMX_3, consists of MA=CH_3NH_3 and $HgCl_3$ ions.[2] The studies carried out by Seliger *et al.*[17] suggest that the disorder of $[CH_3NH_3]^+$ leads to the ferro–paraelectric phase transition that acquires at 333 K. At room temperature, the ferroelectric phase crystallizes in the trigonal symmetry with $P3_2$ space group ($a = b = 7.817$ Å, $c = 9.826$ Å, $\gamma = 120°$, and $Z = 3$; hexagonal cell). As for the paraelectric phase, which acquires above the temperature of phase transition, it crystallizes in the $C2$ space group of the monoclinic system.[17–21] However, the lack of studies that provide an understanding of the electrical behaviors and the charge transport mechanism of the MATM, especially when it presents a ferroelectric nature at room temperature, stirs the need to carry out a study that unveils the physical behavior of the studied material. The challenges to a fundamental understanding of the MATM perovskite stem from its interesting chemical and physical properties and their interplay. In this context, the present paper aims to give an account of the physicochemical, dielectric, and electrical properties of the material MATM. For the physicochemical properties, we present here the results of X-ray powder diffraction, differential scanning calorimetry (DSC) analyses, as well as Raman spectroscopy and scanning electron microscope (SEM) coupled with energy-dispersive X-ray spectroscopy (EDS) results. Moreover, the dielectric and electrical properties are investigated in the current work through impedance spectroscopy measurements as a function of temperature.

2. Experimental

The MATM crystals were prepared at room temperature through a slow solvent evaporation method. The MATM crystals were grown *via* methylamine hydrochloride $CH_5N{\cdot}HCl$ (Sangon Biotech) and mercury(II) chloride $HgCl_2$ (Fluka, 99.5%) dissolved in methanol. We mixed 2 g of $CH_5N{\cdot}HCl$ and 8.0423 g of $HgCl_2$ (with an equal molecular ratio of $CH_5N{\cdot}HCl/HgCl_2$: $n = 0.0296$ mol). These precursors were mixed with methanol in a glass tube, where each of them dissolved immediately without heating. Finally, we mixed both of the solutions in the same tube, and in order to ensure the homogeneity of the resulting solution, the liquid was stirred for a few seconds and then placed in a Petri dish to facilitate the evaporation of the solvent. The Petri dish has been placed in a low-ventilated place, and after 4 days at room temperature without moving or stringing the solution and after the total evaporation of the solvent, colorless monocrystals of MATM were formed. This method is convenient for growing single crystals with high homogeneity and low cost.

Analysis of the microstructure and chemical composition was carried out using scanning electron microscopy (SEM) and energy dispersive spectroscopy (EDS) (MIRA3 FEG microscope), coupled with an Oxford Instrument analyzer with different accelerating voltages.

X-ray powder diffraction (XRD) data were studied at room temperature using a Bruker D8 diffractometer (Cu K_α radiation; 10–90° 2θ range; 0.02° step size), to verify the homogeneity and purity of the MATM compound. The pattern's refinement was carried out by the Rietveld calculation method, using "Fullprof" software.[22]

DSC analysis was performed on a 15 mg sample using the PerkinElmer DSC-7 at temperatures ranging from 273 K to 373 K at an average heating rate of 10 K min^{-1} during the heating and cooling processes.

Raman spectra, performed on different crystals, were recorded at room temperature in the wavenumber range of 50–3500 cm^{-1} using a Renishaw Invia Reflex spectrometer. A 633 nm Ar/Kr laser line was used as the excitation source with a power of 1 mW. The incident light was focused by an ×50 lens with a spot size of around 24 μm in diameter on the surface. In the backscattering configuration, the scattered and emitted light was collected.

A small quantity of MATM crystals was ground in an agate mortar to obtain a fine powder, which was pressed into pellets (1.1 mm in thickness and 8 mm in diameter) under a 5-ton per cm^2 press. Impedance spectroscopy measurements were performed using two electrode configurations. These measurements were performed using an impedance/gain-phase analyzer (Solartron SI-1260), coupled with a dielectric interface (Solartron 1296), and a temperature control system (Linkam LTS420). The data were collected at temperatures between 297 K and 393 K over a wide frequency range from 10^{-1} to 10^6 Hz.

3. Results and discussion

3.1. SEM/EDS analysis

The SEM analysis of the MATM compound was performed on crystals to check the surface morphology of the crystal. The obtained micrographs are represented in Fig. 1(a)–(c), with different magnitudes. The SEM images (a), (b), and (c) confirm the crystalline nature of the crystals of the title compound, and the flat surfaces of the crystals indicate their good quality.[23] Indeed, for many different materials, it was shown that the flat (faceted) surface of the microcrystals is a robust indicator of excellent crystallinity.[23–26] In combination with EDS analysis, which was investigated in different spots as well as for different crystals, the obtained results of the atomic percentage of elements (inset of the EDS (Fig. 2)) indicate that the compound consists of mercury and chloride. Quantitative analysis suggests a surface coverage with atomic ratios Hg/Cl of 27 : 73 for MATM/perovskite. EDS mapping indicates that the observed ratios are very close to the value of 1 : 3, which indicates successful deposition of stoichiometric CH_3NH_3-$HgCl_3$ perovskite. These ratios indicate that the mercury-to-chlor ratio is almost 1 : 3, as one would expect for an ABX_3 perovskite.

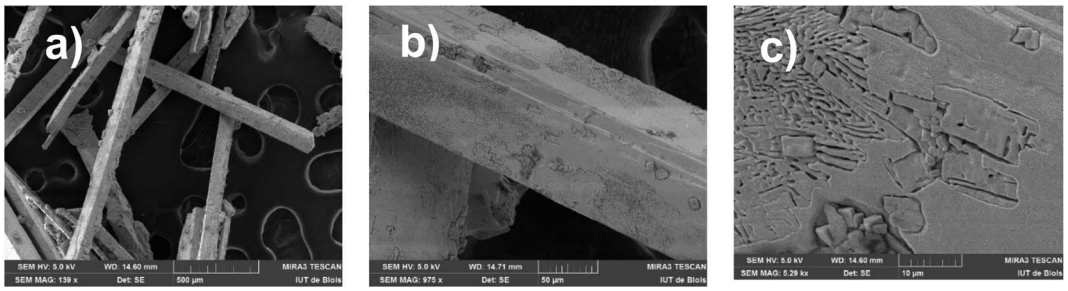

Fig. 1 SEM images of MATM compound.

3.2. X-ray powder diffraction and structure description

To check the crystallinity and purity of the prepared compound, the grown crystals were ground together and underwent an X-ray powder diffraction analysis. Fig. 3 shows the X-ray powder diffraction pattern of the synthesized compound at room temperature. The present phase was fully indexed in the $P3_2$ space group of the trigonal unit cell (hexagonal cell) with $a = b = 7.832(6)$ Å, $c = 9.844\ (2)$ Å, and $Z = 3$. These findings are in good agreement with those reported previously,[18–21] which confirms the perovskite structure of the studied compound. The reliability factors evidenced the goodness of fit, where $R_p = 16.1\%$, $R_{wp} = 14.6\%$, $R_{exp} = 10.2\%$, and $\chi^2 = 2.076$, indicating the high purity of the synthesized sample.

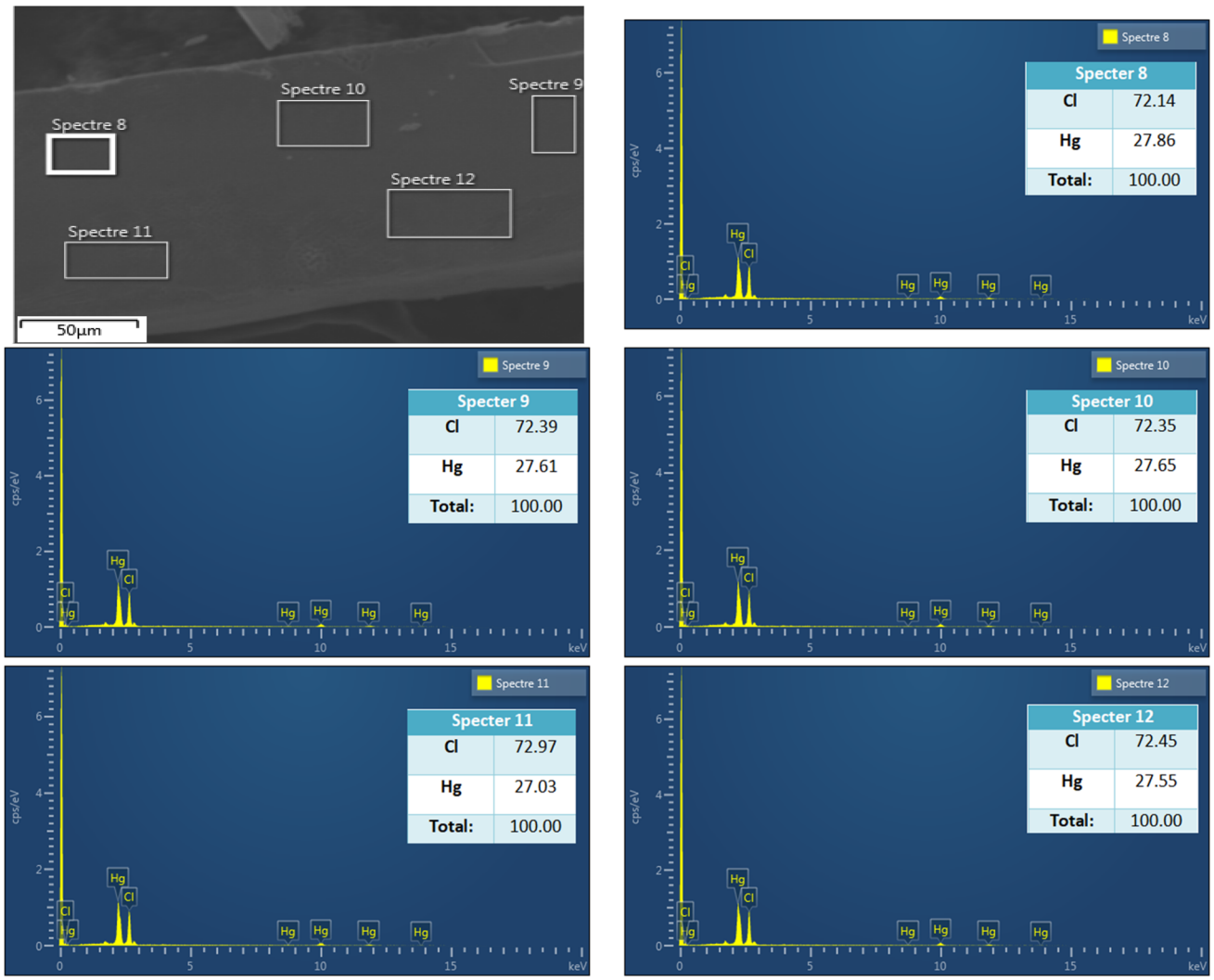

Fig. 2 EDS profile of MATM compound for different crystals with a table of the atomic % of elements (inset figures).

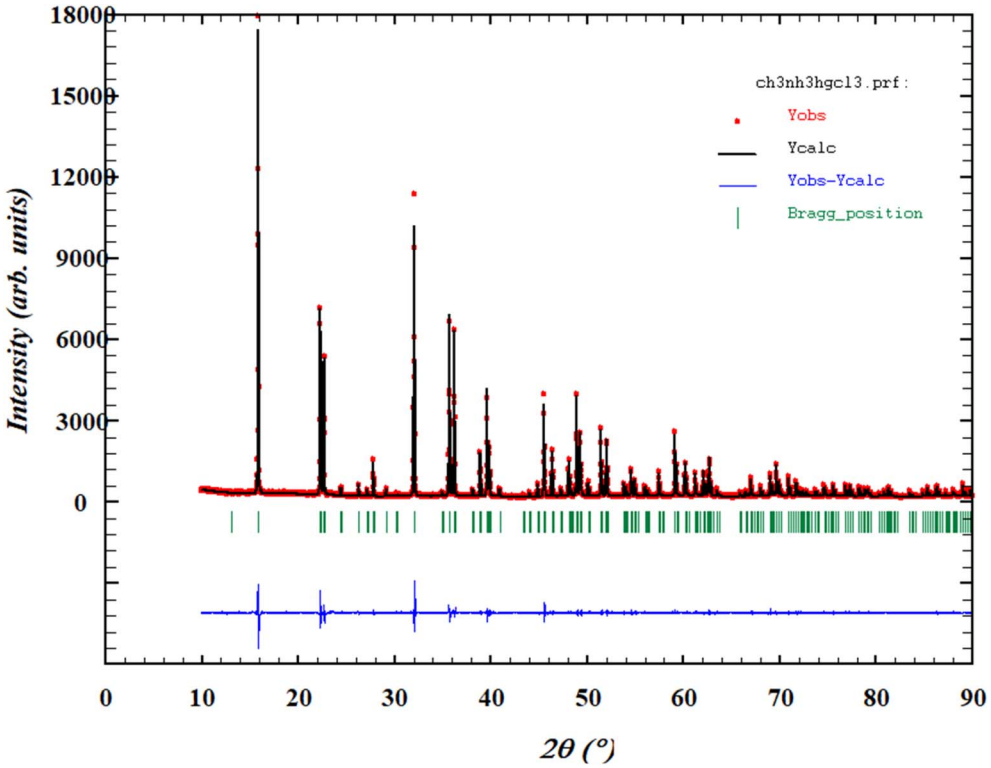

Fig. 3 Rietveld's refinement at room temperature of the X-ray powder diffraction pattern of MATM compound.

It was reported previously[17–21] that the crystal structure of MATM at room temperature was first determined without any consideration of the ferroelectric domains. Close inspection revealed the presence of three-twofold pseudoaxes perpendicular to the threefold axis of the $P3_2$ space group.[18] A decrease in the crystal symmetry, from the trigonal $P3_2$ to the monoclinic $C2$ space group, was detected and linked to a ferro–paraelectric phase transition. This transition is characterized by a loss of the threefold axis in the high-temperature structure. Simultaneously one of the three pseudo-two-fold axes becomes real in the paraelectric phase.[18,21,27]

3.3. Raman spectroscopy

The Raman spectra of MATM's different crystals have been measured in random orientation to ensure the good crystallinity of the material. The spectra were collected at room temperature in the spectral range of 60 to 3500 cm^{-1} and presented in Fig. 4. Observed bands have been interpreted in terms of internal and external vibration modes of $[CH_3NH_3]^+$ and $[HgCl_3]^-$ ions. These modes are assigned by comparison to the observed bands of similar compounds[20,27–29] (see Table 1).

3.4. DSC analysis

The DSC measurement was conducted for the MATM in its crystal form in the temperature range of 273 K to 373 K upon the heating and cooling process at a rate of 10 K min^{-1}. The data show, in Fig. 5, the existence of a reversible peak at 342 ± 2 K and 320 ± 1 K (heating and cooling, respectively). The onset point of the peak on heating and cooling was taken as the phase transition temperature, as schematically shown. This peak is intense and exhibits the characteristics of a first-order phase transition, which was also indicated by the thermal hysteresis $\Delta T = T_1 - T_2$ (see Fig. 5) associated with the transition. The latter is in good agreement with the crystallographic data, where the observed transition does not compromise the group–subgroup relation confirming the first-order type. It has been reported previously that phase transitions are classified into two types, namely order–disorder and displacive transitions. If the entropy value is above 2 J mol^{-1} K^{-1}, the phase transition is mainly considered an order–disorder type.[24,25]

As for the MATM, the enthalpy ΔH is determined after measuring the peak's area, and the entropy ΔS is deduced from the obtained enthalpy.[25] These two factors were determined by the exothermic peak (heating process). Their values are 6.9 K J mol^{-1} and 20.53 J K^{-1} mol^{-1}, respectively. So, the observed phase transition at 342 ± 2 K would be related to the pure order–disorder type.[23] Mainly, the phase transition between distinct crystal structures is due to the organic cations that have a disordered dynamic at high temperatures and freeze at low temperatures.[26] We may conclude that the disorder of $[CH_3NH_3]^+$ is responsible for the ferro–paraelectric nature of the phase transition.[17,18,27]

3.5. Impedance spectroscopy

3.5.1. Electrical properties. The impedance spectroscopy analysis is a well-established method that is critical in

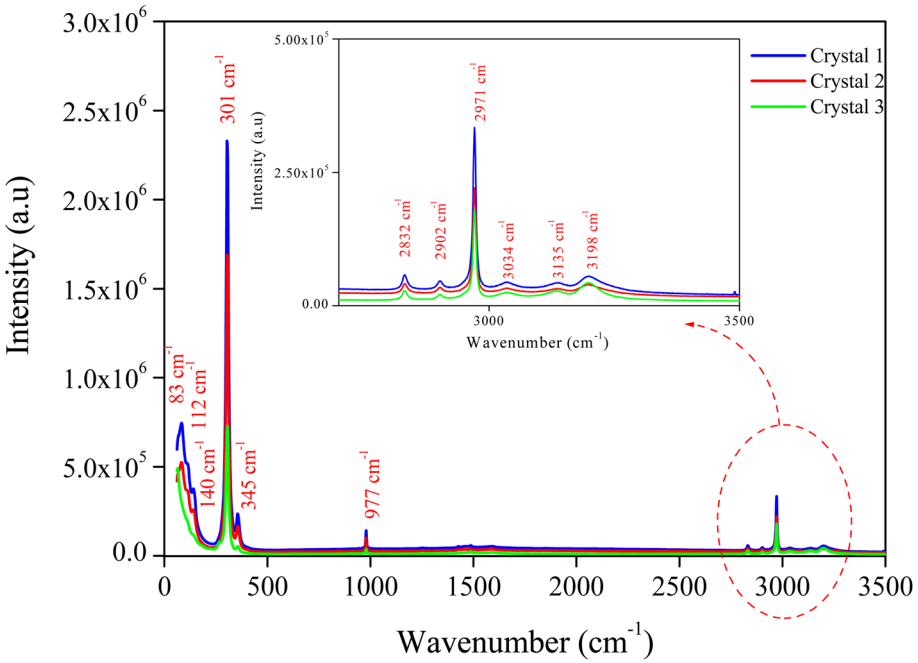

Fig. 4 Raman spectra recorded, at room temperature in the wavenumber 50–3500 cm^{-1}, for different crystals.

Table 1 Assignment of Raman bands for MATM compound[a]

Raman (cm^{-1})	Assignments
83 m	$[CH_3NH_3]^+$ lattice mode
112 m	$[HgCl_3]^-$ bending mode
140 w	
301 vs	$[HgCl_3]^-$ asymmetrical stretching mode
345 w	C–N–C symmetrical bending mode
977 w	C–N symmetrical stretching mode
2832 vw	CH_3 symmetrical stretching mode
2902 vw	
2971 m	CH_3 symmetrical stretching mode
3034 vw	CH_3 asymmetrical stretching mode
3135 vw	NH_3 asymmetrical stretching mode
3198 vw	

[a] vw: very weak; w: weak; m: medium; vs: very strong.

understanding the electrical response of the material under study. It provides information about the motion of ions inside the material, as well as the relaxation time and electrical conductivity.[30]

To suggest a proper equivalent circuit model that well interprets the electrical behavior of the MATM material, we chose to express the experimental data in terms of complex impedances.

Fig. 6(a) and (b) show Nyquist plots, also known as Cole–Cole plots ($-Z''$ *versus* Z'), of the MATM compound over a wide range of temperature and frequency, demonstrating a single depressed semicircle whose center lies below the real axis (Z' axis). The latter is attributed to the existence of single electrical relaxation phenomena[31] and indicates a non-Debye type of relaxation.[32] The presence of a single semicircular arc suggests the dominance of the grain's contribution. The spectra were adequately modeled by a one-cell circuit model, formed by a parallel combination of resistance (R), capacitance (C), and a constant phase element (CPE) (inset Fig. 6(a)). However, interfacial polarization occurs in the spectra even at the temperature of the phase transition (T_{tra} = 343 K). For this reason, we have added a constant phase element (CPE) to the equivalent circuit (inset Fig. 6(b)). The exchange of electrons between the ions of the same molecules takes place. The deformities and imperfections present in the material are responsible for altering the position and distribution of positive and negative space charges. This behavior is caused by the orientation of the methylammonium $[CH_3NH_3]^+$ cations. Under the influence of the applied electric field, positive and negative charges move toward the negative and positive poles of the applied field, respectively. As a result, a large number of dipoles are formed.[30,31] The latter can explain the appearance of the interfacial polarization above T_{tra}.

The resistance of the MATM at each temperature can be determined from the intercept of the semicircular arcs with the real axis (Z'). We may notice that the resistance values decrease with the increase in temperature (inset Fig. 7), accounting for the negative temperature coefficient of the resistances (NTCR). This behavior reveals that the conduction mechanism is thermally activated and the sample presents a semiconductor character.[32–34]

The D. C. conductivity (σ_{DC}) was determined using the following relation:

$$\sigma_{DC} = \frac{t}{A \times R} \quad (1)$$

where "t" and "A" are respectively the thickness and the area of the pellet, and "R" is the grain's resistance.

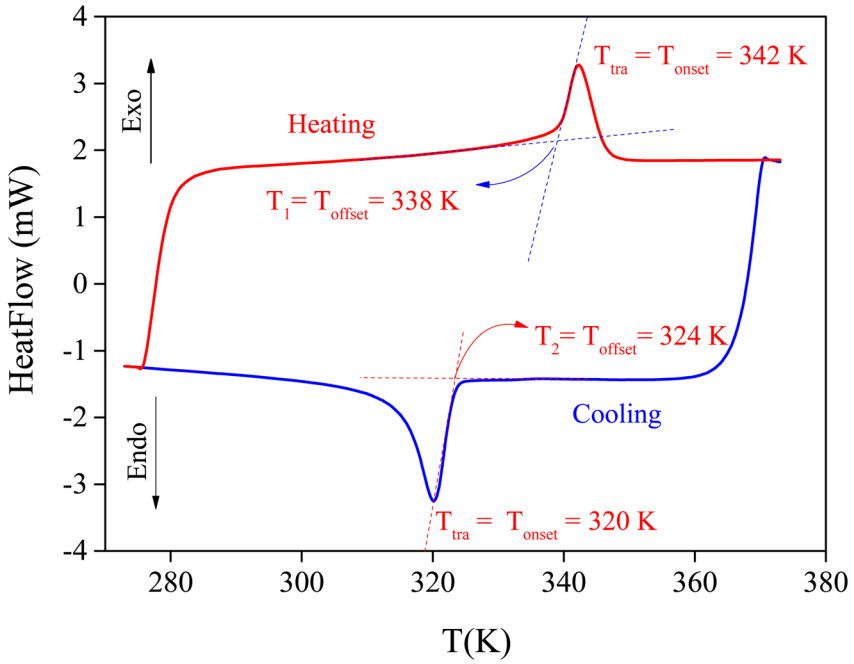

Fig. 5 DSC measurement conducted for the MATM in its crystal form upon heating and cooling process.

The variation of D. C. conductivity as a function of the inverse of temperature is presented in Fig. 7. Its evolution marks an increment with the increase in temperature, obeying Arrhenius' law:

$$\sigma = \sigma_0 \exp\left(-\frac{E_a(\sigma)}{k_B T}\right) \quad (2)$$

where σ_0 is the pre-exponential factor, E_a is the activation energy, k_B is the Boltzmann constant, and T is the temperature.

A change in the slope of the D. C. conductivity curve is observed at $T = 343$ K, which is very close to the temperature of the phase transition detected by DSC analysis. The activation energy values of charge transport resulting from the linear fit are $E_1 = 0.475 \pm 0.03$ eV at low temperatures and $E_2 = 0.454 \pm 0.01$ eV at higher ones. According to DFT calculations performed by Yang *et al.*,[35] as well as results obtained from similar studies,[26] the values of activation energies stand out for the interstitial $[CH_3NH_3]^+$ ions. The distinct activation energies indicate how the orientation of the dipole interacts with the charge carriers, activating the mobility of ions and their diffusion as the temperature increases.[26]

The A. C. conductivity of the sample under study was determined, using the impedance's real Z' and imaginary Z'' measured values, by applying the following relation:

$$\sigma_{AC} = \left(\frac{t}{A}\right)\left(\frac{Z'}{Z'^2 + Z''^2}\right) \quad (3)$$

The evolution of A. C. conductivity (σ_{AC}), as a function of frequency and in the studied temperature range, is presented in Fig. 8. Two regions can be identified in these spectra. The first, located in the low frequencies, appears as a plateau, which is attributed to the conductivity behavior, namely D. C. conductivity. The second, located at higher frequencies, is known as the "conductivity scattered area", where the conductivity increases due to the mobility of charge carriers with the increase in frequency.[36] This behavior can be described by Jonscher's universal power law:[37]

$$\sigma_{AC} = \sigma_{DC} + B\omega^{s(T)} \quad (4)$$

where "B" is the temperature-dependent factor and $s(T)$ is the power exponent that represents the degree of interaction between mobile ions and the surrounding environment ($0 < s < 2$).[34,38]

In previous works, diverse conduction models were reported, mainly classified into two distinct processes: the classical hopping over a barrier and the quantum tunneling effect. However, over the years, some modifications were performed. The final proposed models are quantum mechanical tunneling (QMT), correlated barrier hopping (CBH), non-overlapping small polaron tunneling (NSPT), and overlapping large polaron tunneling (OLPT).[39]

These models were proposed to correlate the conduction mechanism of the A. C. conductivity with the behavior of $s(T)$ as a function of temperature.

The thermal variation of $s(T)$ is provided in the inset of Fig. 8. It is worth noting that $s(T)$ decreases with increasing temperature before increasing again after the phase transition temperature. This behavior coincides with the CBH model for $T < T_{tra}$ (ferroelectric phase) and with the NSPT model for $T > T_{tra}$ (paraelectric phase).

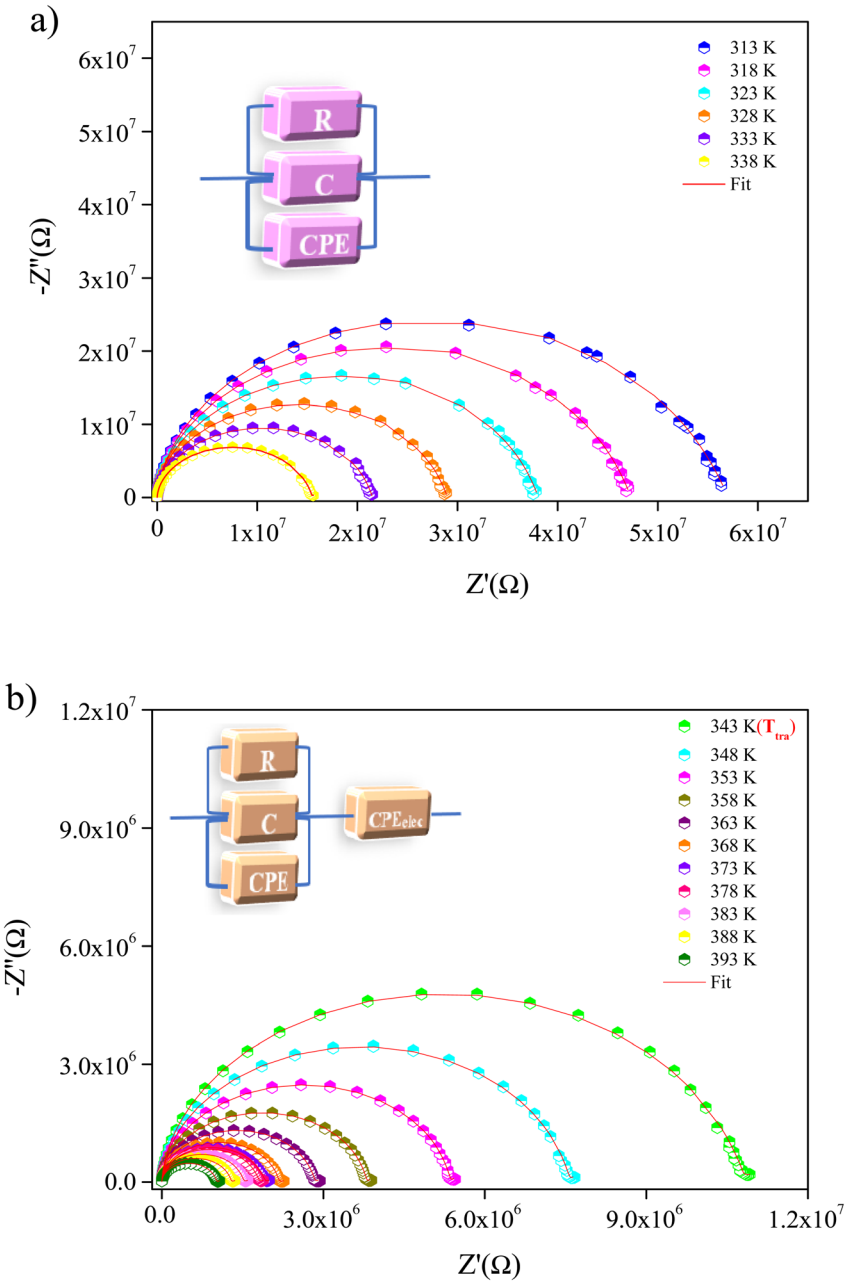

Fig. 6 Nyquist plot of MATM compound, at different temperatures, (a) before and (b) after the temperature of phase transition.

3.5.2. Dielectric properties. Fig. 9(a) and (b) show the temperature dependence of the real ε' and imaginary ε'' parts of the complex electric permittivity, respectively. The measurements were made at various frequencies in the temperature range 313–393 K. The real part's curve (Fig. 9(a)) shows a prominent dielectric peak around 343 K, which is associated with the ferro–paraelectric phase transition. In addition, the curve of the imaginary part ε'' (Fig. 9(b)) reveals that the values of ε'' are almost constant for $T < 343$ K. This behavior can be interpreted by the halting of the atomic motion, induced by the low thermal energy of the charge carriers, leaving them unable to follow the direction of the electric field. However, above 343 K, the values of ε'' start to increase with the increase in temperature, indicating that the charge carriers have gained sufficient thermal energy to follow the direction of the electric field.[40,41] As the MATM was reported previously as a ferroelectric material, this fact triggers the need to investigate whether it is a classic ferroelectric or a relaxor one. It is evident in Fig. 9(a) that the ferro–paraelectric transition temperature ($T_C = 343$ K) is independent of frequency, revealing that the MATM is a classic ferroelectric.[42,43] The broadened peak that appears in the real part ε' indicates that the transition is of the diffuse type, which is an important feature of a disordered perovskite structure.[44] Fig. 10 represents the plot of Curie–Weiss $(1/\varepsilon'_r)$ as a function of temperature at a fixed frequency of 1.25 MHz. The

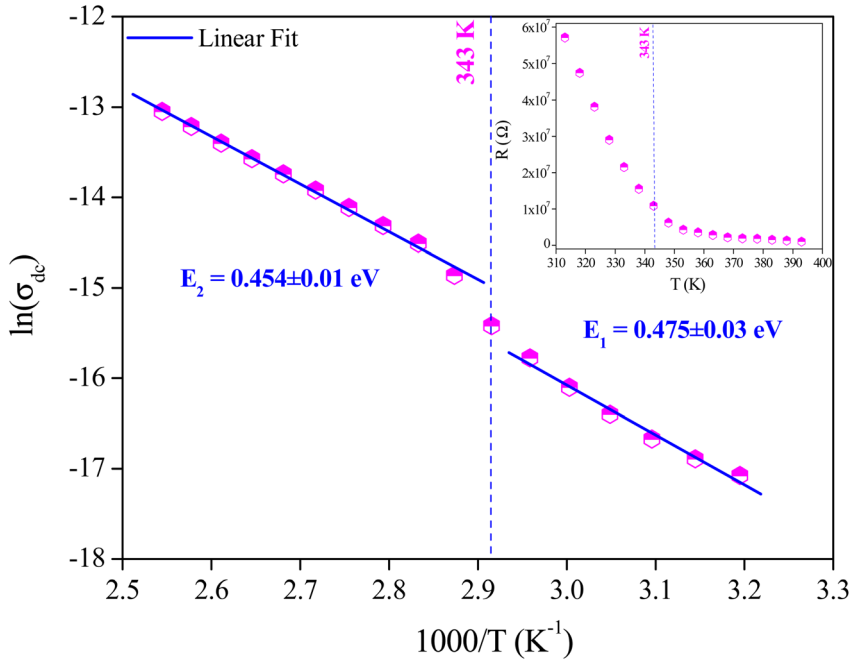

Fig. 7 Variation of D. C. conductivity of the grains as a function of (1000/T), and variation of grains resistance as a function of temperature (inset).

latter appears as a straight line just above the temperature of the phase transition.

The degree of disorder in the ferroelectric MATM was evaluated using an empirical formula developed by Uchino and Nomura:[45]

$$\frac{1}{\varepsilon'_{r}} - \frac{1}{\varepsilon'_{r\,max}} = \frac{(T - T_c)^{\gamma}}{C} \quad (5)$$

where ε'_{r} is the relative dielectric constant at temperature T, $\varepsilon'_{r\,max}$ is the maximum value at Curie–Weiss temperature T_c, C is the Curie–Weiss constant, and γ is the factor of diffuseness ($1 < \gamma < 2$). When the 1 and 2 limiting values of γ are used, the Curie–Weiss equation is reduced, yielding the classical ferroelectric and the ideal relaxer ferroelectric.[44] In our case, the γ values determined for different frequencies were found to be close to

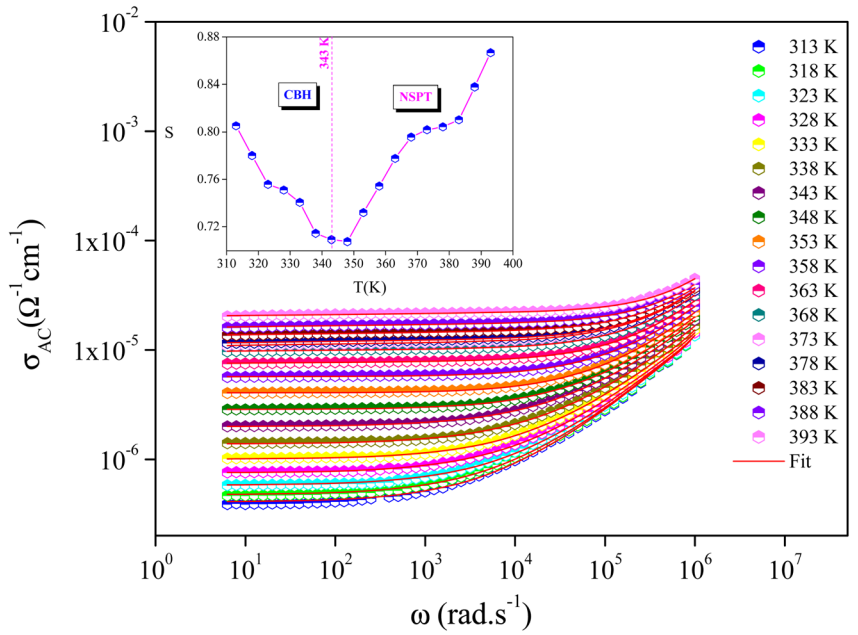

Fig. 8 Variation of σ_{AC} with angular frequency at different temperatures, and temperature dependence of the frequency exponent s (inset Fig. 8).

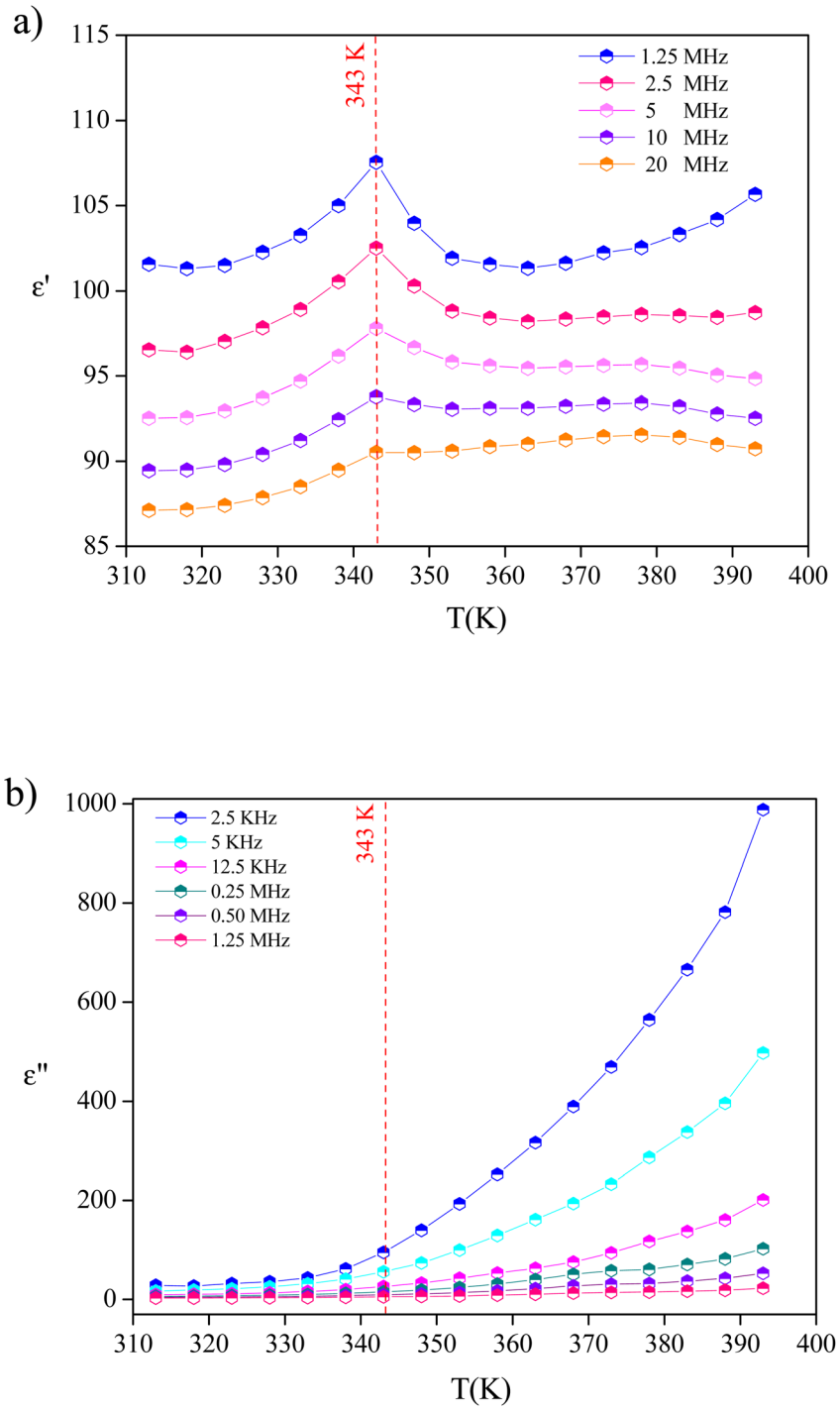

Fig. 9 (a) Real and (b) imaginary parts of permittivity *vs.* temperature at selected frequencies.

the unit. So, we may conclude that the MATM compound is a classical ferroelectric.

The temperature dependence of dielectric responses revealed the presence of anomalous dielectric behavior at 343 K (identified as a ferro–paraelectric phase transition), which is normally the temperature at which dielectric relaxation occurs. Thus, we now report the frequency dependence of the dielectric response at different temperatures, which is expressed in the form of the complex dielectric constant $\varepsilon^*(\omega)$ that can be expressed as the following:

$$\varepsilon^*(\omega) = \varepsilon'(\omega) - j\varepsilon''(\omega) \quad (6)$$

where $\varepsilon'(\omega)$ is the real part of the complex permittivity that represents the stored energy, and $\varepsilon''(\omega)$ is the imaginary part of the complex permittivity as well as the energy dissipation of the applied electric field as polarization.[30]

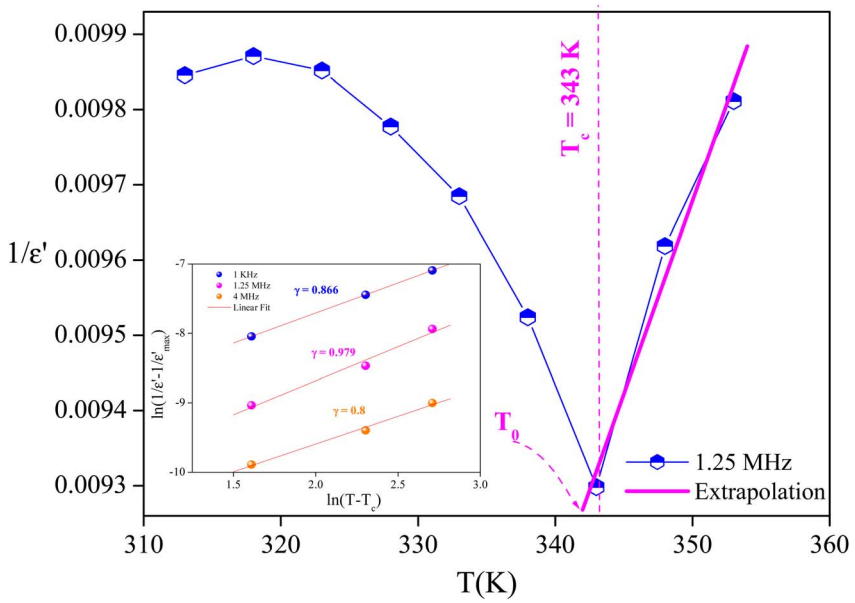

Fig. 10 Curie–Weiss plot ($1/\varepsilon'_r$), as a function of temperature at a fixed frequency (1.25 MHz).

Fig. 11(a) and (b) depict the investigation and demonstration of the variation of the dielectric constant's real and imaginary parts as a function of frequency. We may notice that the dielectric constant is large (reaching 8×10^3 for $\varepsilon'(\omega)$ and 3.7×10^5 for $\varepsilon''(\omega)$) in the low-frequency region and decreases gradually with the increase of frequency to remain constant at a higher frequency. Such behavior indicates a large dielectric dispersion behavior and a thermally activated nature of the dielectric relaxation.[45–47] Each of $\varepsilon'(\omega)$ and $\varepsilon''(\omega)$ plays a noteworthy role in defining the ionic conduction process, which is mainly ruled by ionic, electronic, orientational, and interfacial polarization. The behavior of the dielectric response in the low-frequency region was found to be governed by orientational polarization and interfacial polarization, which confirms the non-Debye behavior.[30] As for the high-frequency region, the ionic and electronic polarizations are responsible for lowering the value of the dielectric constant.[30,48]

To study the variation of the dielectric constant *versus* frequency in the studied temperature range, the modified Cole–Cole model with D. C. conductivity was used, where a correction term has been added. According to the modified Cole–Cole model, the complex permittivity can be stated as:[30,48,49]

$$\varepsilon^* = \varepsilon_\infty + \frac{(\varepsilon_s - \varepsilon_\infty)}{1 + j(\omega\tau)^\beta} - \frac{j\sigma^*}{\varepsilon_0 \omega^m} \quad (7)$$

where σ^* is the complex conductivity, $\varepsilon_s$is the static and ε_∞ is the infinite frequency dielectric constants, ω is the angular frequency, τ is a time constant, β is the modified Cole–Cole parameter, and m is the frequency exponent.

From the previous relation, the complex permittivity can be decomposed into the real $\varepsilon'(\omega)$ and $\varepsilon''(\omega)$ imaginary parts can be expressed as the following:

$$\varepsilon' = \varepsilon_\infty + \frac{(\varepsilon_s - \varepsilon_\infty)\left(1 + (\omega\tau)^\beta \cos\left(\frac{\beta\pi}{2}\right)\right)}{1 + 2(\omega\tau)^\beta \cos\left(\frac{\beta\pi}{2}\right) + (\omega\tau)^{2\beta}} + \frac{\sigma_{sp}}{\varepsilon_0 \omega^m} \quad (8)$$

$$\varepsilon'' = \frac{(\varepsilon_s - \varepsilon_\infty)(\omega\tau)^\beta \sin\left(\frac{\beta\pi}{2}\right)}{1 + 2(\omega\tau)^\beta \cos\left(\frac{\beta\pi}{2}\right) + (\omega\tau)^{2\beta}} + \frac{\sigma_{fc}}{\varepsilon_0 \omega^m} \quad (9)$$

where σ_{sp} is the conductivity due to the free charge carrier (known by D. C. conductivity) and σ_{fc} is the conductivity due to the space charges (localized charges).

The experimental data of real and imaginary parts were fitted with the modified Cole–Cole equation using the previous equations.

To gain insight into the relaxation procedure in MATM, detailed complex modulus ($M^* = M' + jM''$) spectra have been studied. The imaginary part M'' of the electric modulus as a function of angular frequencies in the studied temperature range is illustrated in Fig. 12(a). These spectra reveal a single peak's presence, confirming the studied material's single relaxation phenomenon. These findings are in good agreement with those of the Nyquist plots.

The observed peaks are slightly asymmetric at each temperature, and they are rather wider than the peaks of Debye. The enlargement points out the spread of relaxation with different meantime constants, confirming the non-Debye relaxation of the MATM.[41,49,50] In addition, with the increase in temperature, the position of the peaks marks a shift toward the higher frequencies. These observations were confirmed by the analysis of the single peak characteristic using the Bergman equation, which is stated as follows:

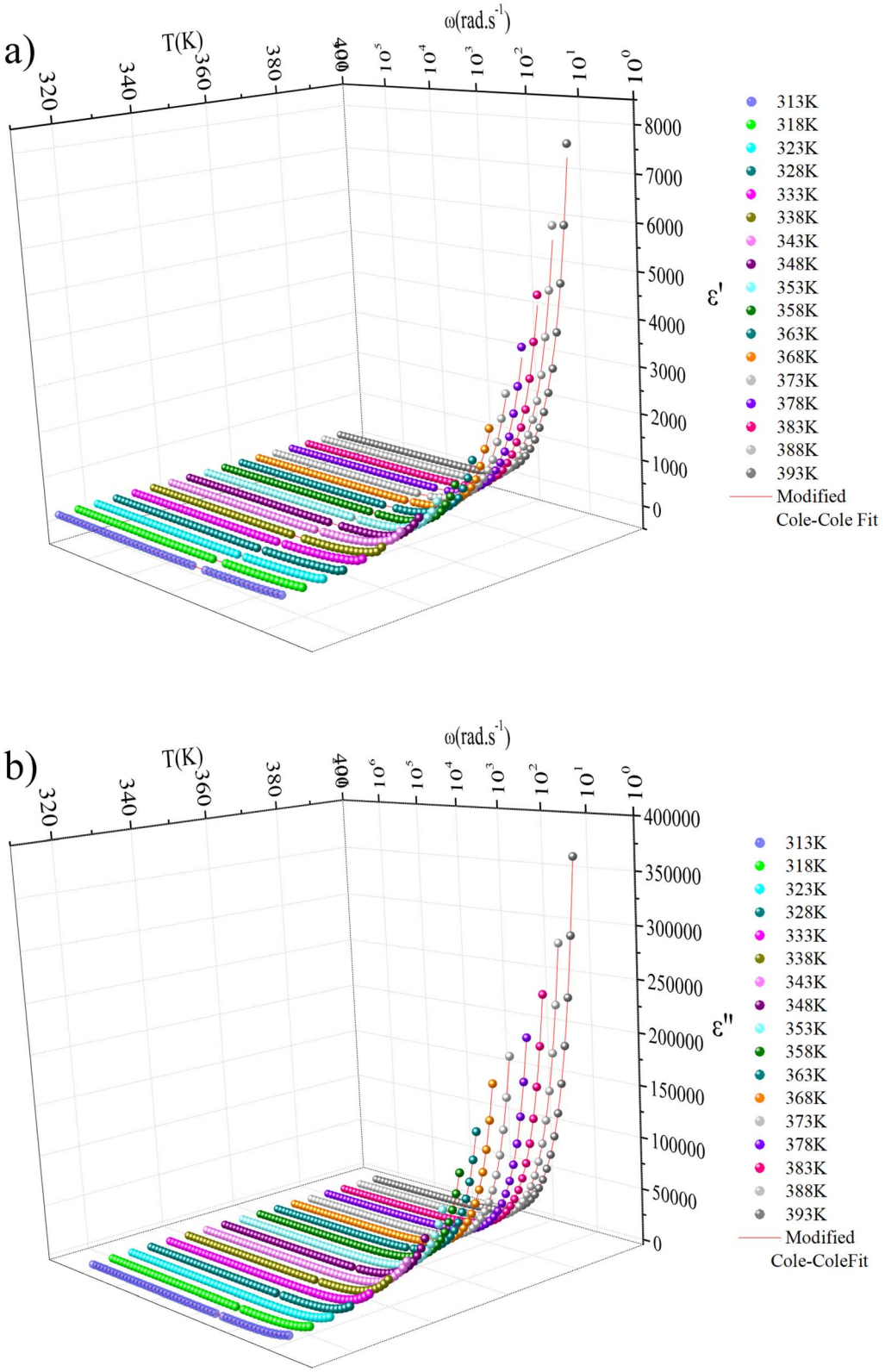

Fig. 11 (a) Real and (b) imaginary parts of permittivity *vs.* frequency at selected temperatures.

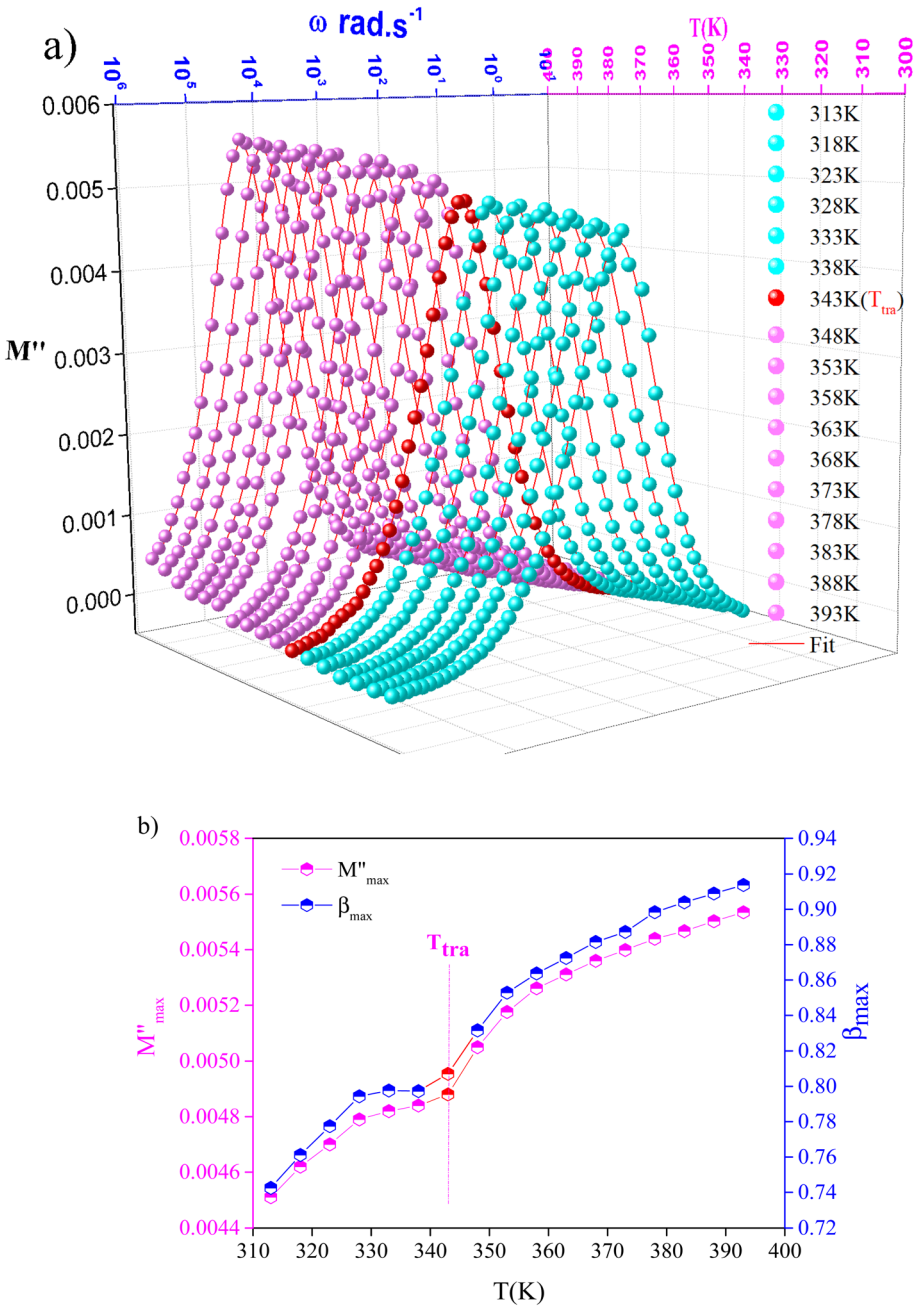

Fig. 12 Variation of (a) modulus spectra (M'') *vs.* frequency and (b) parameters (M''_{max}, β) as a function of temperature.

$$M'' = \frac{M''_{max}}{\left((1-\beta') + (\beta'/(1+\beta'))\left[\beta'\left(\frac{\omega_{max}}{\omega}\right) + \left(\frac{\omega}{\omega_{max}}\right)^{\beta'}\right]\right)} \quad (10)$$

where M''_{max} is the modulus maximum associated with the frequency noted by ω_{max}, β' is known by the Kohlrausch parameter ($0 < \beta' < 1$).

Fig. 12(b) represents the variation of each M''_{max} and β' values, as a function of temperature. The variation of these two parameters reveals the existence of two distinct regions with a change in slope around the same temperature as the detected phase transition. The behavior of these factors reveals that the mechanism of the observed phase transition may be described as an order–disorder transition, and the movement of $[CH_3NH_3]^+$ cations is at least between two energetically equivalent positions.[51] These findings are in good agreement with those of the DSC analysis.

4. Conclusions

Methylammonium Trichloro-Mercurate (MATM) crystals were grown through a slow evaporation method. Several complementary techniques, along with the XRPD analysis, were brought together to investigate the surface morphology,

stoichiometry, and purity of the MATM in its crystal and powder forms. SEM analysis confirmed the crystalline nature and the flat surfaces of the crystals, indicating the good quality of the MATM crystals. EDS analysis revealed a surface coverage with Hg/Cl atomic ratios of 27 : 73, indicating a successful deposition of stoichiometric MATM perovskite. These ratios show that the mercury-to-chlorine ratio is almost 1 : 3, as expected for an ABX_3 perovskite. As for the vibrational analysis, Raman spectra recorded at room temperature have given information about the internal and external vibration modes of $[CH_3NH_3]^+$ and $[HgCl_3]^-$ ions. As for thermal analysis, the DSC revealed the existence of a reversible peak at 342 ± 2 K and 320 ± 1 K upon the heating and cooling processes, respectively. The latter is associated with a first-order phase transition of an order–disorder nature, produced from the disorder of $[CH_3NH_3]^+$ ions. The electrical, dielectric, and relaxation properties of the MATM hybrid perovskite are studied using impedance spectroscopy to characterize the material's intrinsic electrical behavior. Following the structural aspects, this behavior is interpreted, establishing a link between the nature of the migrating species and their impact on the macroscopic properties. The Nyquist plots revealed the existence of single electrical relaxation phenomena, indicating a non-Debye type relaxation, and the presence of a single semicircular arc suggests the dominance of the grain's contribution. These plots were satisfactorily fitted with the one-cell *R*/*C*/CPE circuit model, with the exception of adding a CPE element in series from the temperature of phase transition. The latter was interpreted by the formation of a significant number of dipoles, creating an interfacial polarization. A change in the slope of the D. C. conductivity curve is observed around the same temperature of the phase transition detected by DSC analysis. The activation energy values of charge transport are $E_1 = 0.475 \pm 0.03$ eV ($T < T_{tra}$) and $E_2 = 0.454 \pm 0.01$ eV ($T > T_{tra}$). These values were found to stand out for the interstitial $[CH_3NH_3]^+$ ions. In addition, the A. C. conductivity was successfully described through Jonscher's power law. The variation of the deduced $s(T)$ indicates that the CBH model interprets the charge transport mechanism in the MATM well (for $T < T_{tra}$), but switches to an NSPT model above T_{tra}. As for the dielectric study, as a function of temperature, it provides arguments for the existence of ferroelectricity, revealing the classic ferroelectric nature of the studied material. However, it confirms the findings of the electrical study as a function of frequency, where the space charge and free charge conductivity were determined through the modified Cole–Cole plot.

The presented results provide insights into the correlation between the properties of this material, leading us to conclude that MATM is a feasible perovskite that could be used in energy-harvesting systems.

Conflicts of interest

There are no conflicts to declare.

Acknowledgements

This work is financially supported by the Ministry of Higher Education and Scientific Research of Tunisia.

References

1 A. Mhiri, F. Krichen, A. Oueslati, J. Lhoste, F. Goutenoire, M. Gargouri and A. Bulou, Synthesis, structural characterization, and spectroscopic studies of bis tetramethylammonium hexabromostannate $[N(CH_3)_4]_2SnBr_6$, *J. Alloys Compd.*, 2019, **772**, 546–556, DOI: 10.1016/j.jallcom.2018.09.158.

2 I. Borriello, G. Cantele and D. Ninno, Finding new perovskite halides via machine learning, *Phys. Rev. B: Condens. Matter Mater. Phys.*, 2008, **77**, 235214, DOI: 10.1103/PhysRevB.77.235214.

3 I. Chaabane, F. Hlel and K. Guidara, Electrical study by impedance spectroscopy of the new compound $[C_{12}H_{17}N_2]_2CdCl_4$, *J. Alloys Compd.*, 2008, **461**, 495–500, DOI: 10.1016/j.jallcom.2007.07.031.

4 A. Kojima, K. Teshima, Y. Shirai and T. Miyasaka, Organometal Halide Perovskites as Visible-Light Sensitizers for Photovoltaic Cells, *J. Am. Chem. Soc.*, 2009, **131**, 6050–6051, DOI: 10.1021/ja809598r.

5 R. H. Petrosova, O. I. Kucheriv, S. Shova and I. A. Gural'skiy, Aziridinium cation templating 3D lead halide hybrid perovskites, *Chem. Commun.*, 2022, **58**(38), 5745–5748, DOI: 10.1039/D2CC01364A.

6 M. Mączka, M. Ptak, A. Gągor, D. Stefańska, J. K. Zaręba and A. Sieradzki, Methylhydrazinium Lead Bromide: Noncentrosymmetric Three-Dimensional Perovskite with Exceptionally Large Framework Distortion and Green Photoluminescence, *Chem. Mater.*, 2020, **32**(4), 1667–1673, DOI: 10.1021/acs.chemmater.9b05273.

7 M. Maçzka, A. Gagor, J. K. Zareba, D. Stefanska, M. Drozd, S. Balciunas, M. Šimenas, J. Banys and A. Sieradzki, Three-dimensional perovskite methylhydrazinium lead chloride with two polar phases and unusual second-harmonic generation bistability above room temperature, *Chem. Mater.*, 2020, **32**(9), 4072–4082, DOI: 10.1021/acs.chemmater.0c00973.

8 M. Saliba, T. Matsui, K. Domanski, J. Y. Seo, A. Ummadisingu, S. M. Zakeeruddin, M. Grätzel, *et al.*). Incorporation of rubidium cations into perovskite solar cells improves photovoltaic performance, *Science*, 2016, **354**(6309), 206–209, DOI: 10.1126/science.aah5557.

9 S. X. Tao, X. Cao and P. A. Bobbert, Accurate and efficient band gap predictions of metal halide perovskites using the DFT-1/2 method: GW accuracy with DFT expense, *Sci. Rep.*, 2017, **7**(1), 1–9, DOI: 10.1038/s41598-017-14435-4.

10 C. Bao, J. Yang, S. Bai, W. Xu, Z. Yan, Q. Xu, F. Gao, *et al.*). High Performance and Stable All-Inorganic Metal Halide Perovskite-Based Photodetectors for Optical Communication Applications, *Adv. Mater.*, 2018, **30**(38), 1–8, DOI: 10.1002/adma.201803422.

11 J. Sun, J. Wu, X. Tong, F. Lin, Y. Wang and Z. M. Wang, Organic/Inorganic Metal Halide Perovskite Optoelectronic Devices beyond Solar Cells, *Adv. Sci.*, 2018, **5**(5), 1700780, DOI: 10.1002/advs.201700780.

12 Y. Liu, Z. Yang, D. Cui, X. Ren, J. Sun, X. Liu, S. Liu, *et al.*). Two-Inch-Sized Perovskite $CH_3NH_3PbX_3$ (X = Cl, Br, I) Crystals: Growth and Characterization, *Adv. Mater.*, 2015, **27**(35), 5176–5183, DOI: **10.1002/adma.201502597**.

13 J. M. Kadro, K. Nonomura, D. Gachet, M. Grätzel and A. Hagfeldt, Facile route to freestanding CH3NH3PbI3 crystals using inverse solubility, *Sci. Rep.*, 2015, **5**, 1–6, DOI: **10.1038/srep11654**.

14 M. A. Afroz, C. A. Aranda, N. K. Tailor, P. Yukta Yadav, M. M. Tavakoli, S. Satapathi, *et al.*). Impedance Spectroscopy for Metal Halide Perovskite Single Crystals: Recent Advances, Challenges, and Solutions, *ACS Energy Lett.*, 2021, **6**(9), 3275–3286, DOI: **10.1021/acsenergylett.1c01099**.

15 K. Mencel, P. Durlak, M. Rok, R. Jakubas, J. Baran, W. Medycki, A. Piecha-Bisiorek, *et al.*). Widely used hardly known. An insight into electric and dynamic properties of formamidinium iodide, *RSC Adv.*, 2018, **8**(47), 26506–26516, DOI: **10.1039/c8ra03871f**.

16 M. M. Lee, J. Teuscher, T. Miyasaka, T. N. Murakami and H. J. Snaith, Efficient hybrid solar cells based on meso-superstructured organometal halide perovskites, *Science*, 2012, **338**(6107), 643–647, DOI: **10.1126/science.1228604**.

17 J. Seliger, V. Zagar, R. Blinc, F. Milia and S. Giannacopoulos, Proton ^{14}N double resonance study of the ferroelectric phase transition in $(CH_3NH_3)HgC1_3$, *Solid State Commun.*, 1986, **59**(12), 877–879, DOI: **10.1016/0038-1098(86)90648-4**.

18 H. Fuess, M. Körfer, H. Arend and R. Kind, A new ferroelectric compound: Methylammonium trichloromercurate $(CH_3NH_3HgCl_3)$, *Solid State Commun.*, 1985, **56**(1), 137–139, DOI: **10.1016/0038-1098(85)90551-4**.

19 F. Milia and M. Voudouris, $^{35}C1$ NQR Study of the low temperature transition in ferroelectric $(CH_3NH_3)HgCl_3$, *Solid State Commun.*, 1986, **60**(3), 261–262, DOI: **10.1016/0038-1098(86)90460-6**.

20 M. Daub, R. Stroh, H. Hillebrecht, M. Koerfer, H. Fuess, M. Prager, E. J. Zehnder, M. A. Hossain, J. P. Srivastava, H. D. Bist, P. K. Khulbe, Z. T. Jiang, B. D. James, J. Liesegang, K. L. Tan, R. Gopalakrishnan and I. Novak, Raman spectroscopic evidence of the phase transition in $CH_3NH_3HgCl_3$, *Phys. Status Solidi A*, 1991, **123**(2), 535–538, DOI: **10.1002/pssa.2211230218**.

21 Y. Ishibashi and V. Dvorak, Structural Phase Transitions in $CH_3NH_3HgCl_3$, *J. Phys. Soc. Jpn.*, 1989, **58**(12), 4493–4495, DOI: **10.1143/JPSJ.58.4493**.

22 R. A. Young, P. E. Mackie and R. B. von. Dreele, Application of the Pattern-Fitting Structure-Refinement Method to X-ray Powder Diffractometer Patterns, *J. Appl. Crystallogr.*, 1977, **10**, 262–269, DOI: **10.1107/S0021889877013466**.

23 M. H. Mrada, I. Feddaoui, M. S. M. Abdelbaky, S. García-Granda and C. Ben Nasr, Elaboration, crystal structure, characterization and DFT calculation of a new Hg(II) inorganic-organic hybrid salt $[C_6H_{16}N_2O]HgCl_4$, *J. Solid State Chem.*, 2020, **286**, 121280, DOI: **10.1016/j.jssc.2020.121280**.

24 P. Szklarz, M. Owczarek, G. Bator, T. Lis, K. Gatner and R. Jakubas, Crystal structure, properties and phase transitions of morpholinium tetrafluoroborate $[C_4H_{10}NO][BF_4]$, *J. Mol. Struct.*, 2009, **929**(1–3), 48–57, DOI: **10.1016/j.molstruc.2009.04.014**.

25 I. Gharbi, A. Oueslati, K. Guidara and B. Louati, Ionic conductivity and conduction mechanism of $CsZnPO_4$ compound, *Ionics*, 2019, **25**, 3991–4001, DOI: **10.1007/s11581-019-02954-1**.

26 R. E. Patru, H. Khassaf, I. Pasuk, M. Botea, L. Trupina, C. Ganea, L. Pintilie and I. Pintilie, Tetragonal – Cubic Phase Transition and Low-Field Dielectric Properties of CH 3 NH 3 PbI 3 Crystals, *Materials*, 2021, **14**(15), 4215, DOI: **10.3390/ma14154215**.

27 Z. T. Jiang, B. D. James, J. Liesegang, K. L. Tan, R. Gopalakrishnan and I. Novak, Investigation of the ferroelectric phase transition in $(CH_3NH_3)HgCl_3$, *J. Phys. Chem. Solids*, 1995, **56**(2), 277–283, DOI: **10.1016/0022-3697(94)00176-6**.

28 M. A. Hossain, J. P. Srivastava, H. D. Bist and P. K. Khulbe, Raman spectroscopic evidence of the phase transition in $CH_3NH_3HgCl_3$, *Phys. Status Solidi A*, 1991, **123**(2), 535–538, DOI: **10.1002/pssa.2211230218**.

29 F. Lambarki, A. Ouasri, A. Rhandour, M. Saadi, L. El Ammari and L. Hajji, Structural, vibrational and electrical studies of tetramethylammonium trichloromercurate $[(CH_3)_4N]HgCl_3$, *J. Mol. Struct.*, 2018, **1173**, 865–875, DOI: **10.1016/j.molstruc.2018.07.051**.

30 P. Sengupta, P. Sadhukhan, A. Ray, R. Ray, S. Bhattacharyya and S. Das, Temperature and frequency dependent dielectric response of $C_3H_7NH_3$ PbI_3: a new hybrid perovskite, *J. Appl. Phys.*, 2020, **127**(20), 204103, DOI: **10.1063/1.5142810**.

31 J. L. C. Huamán, Perovskite Ceramics Recent Advances and Emerging Applications, in *Perovskite Ceramics*, ed. J. L. C. Huamán and V. A. G. Rivera, 1st edn, 2023. DOI: **10.1016/c2020-0-03937-x**.

32 M. Abbassi, R. Ternane, I. Sobrados, A. Madani, M. Trabelsi-Ayadi and J. Sanz, Ionic conductivity of apatite-type solid electrolyte ceramics $Ca_{2-x}Ba_xLa_4Bi_4(SiO_4)_6O_2$ $(0 \leq x \leq 2)$, *Ceram. Int.*, 2013, **39**(8), 9215–9221, DOI: **10.1016/j.ceramint.2013.05.026**.

33 C. Thirmal, P. Murugavel and V. Subramanian, Impedance spectroscopic analysis of the organic ferroelectric - Diisopropylammonium bromide (DIPAB), *Curr. Appl. Phys.*, 2014, **14**(5), 688–690. **10.1016/j.cap.2014.02.018**.

34 Y. Pu, Z. Dong, P. Zhang, Y. Wu, J. Zhao and Y. Luo, Dielectric, complex impedance and electrical conductivity studies of the multiferroic $Sr_2FeSi_2O_7$-crystallized glass-ceramics, *J. Alloys Compd.*, 2016, **672**, 64–71, DOI: **10.1016/j.jallcom.2016.02.137**.

35 D. Yang, W. Ming, H. Shi, L. Zhang and M. H. Du, Fast Diffusion of Native Defects and Impurities in Perovskite Solar Cell Material $CH_3NH_3PbI_3$, *Chem. Mater.*, 2016, **28**(12), 4349–4357, DOI: **10.1021/acs.chemmater.6b01348**.

36 G. F. Pike, AC Conductivity of Scandium Oxide and a New Hopping Model for Conductivity, *Phys. Rev. B: Solid State*, 1972, **6**, 1572, DOI: **10.1103/PhysRevB.6.1572**.

37 A. Jonscher, The 'universal' dielectric response, *Nature*, 1977, **267**, 673–679, DOI: **10.1038/267673a0**.

38 I. Gharbi, A. Oueslati and K. Guidara, Alternating current conduction mechanisms of $RbMgPO_4$ compound, *Mater. Res. Bull.*, 2018, **100**, 1–6, DOI: 10.1016/j.materresbull.2017.11.058.

39 C. B. Mohamed, K. Karoui, F. Jomni, K. Guidara and A. B. Rhaiem, Electrical properties and conduction mechanism of $[C_2H_5NH_3]_2CuCl_4$ compound, *J. Mol. Struct.*, 2015, **1082**, 38–48, DOI: 10.1016/j.molstruc.2014.11.006.

40 S. Hajlaoui, I. Chaabane, J. Lhoste, A. Bulou and K. Guidara, Structural characterization, vibrational spectroscopy accomplished with DFT calculation, thermal and dielectric behaviors in a new organic–inorganic tertrapropylammonium aquapentachlorostannate dihydrate compound, *J. Alloys Compd.*, 2016, **679**, 302–315, DOI: 10.1016/j.jallcom.2016.04.015.

41 I. Gharbi, A. Oueslati, M. H. Dhaou and M. Gargouri, Investigation of ferroelectric phase transitions in $TlZnPO_4$ stuffed tridymite compound, *J. Solid State Chem.*, 2022, **308**(2021), 122886, DOI: 10.1016/j.jssc.2022.122886.

42 S. Aydi, A. Amouri, S. Chkoundali and A. Aydi, Lead-free ferroelectric $Na_{1-x}Sr_x$ $(Sn_{0.25}Ti_{0.75})$ $xNb_{1-x}O_3$ system ($0.1 \leq x \leq 0.4$) XRD, dielectric, and Raman properties, *Ceram. Int.*, 2017, **43**(15), 12179–12185, DOI: 10.1016/j.ceramint.2017.06.076.

43 M. Abdessalem, I. Kriaa, A. Aydi and N. Abdelmoula, Large electrocaloric effect in lead-free $Ba_{1-x}Ca_xTi_{1-y}ZryO_3$ ceramics under strong electric field at room-temperature, *Ceram. Int.*, 2018, **44**(12), 13595–13601, DOI: 10.1016/j.ceramint.2018.04.194.

44 L. Khemakhem, A. Kabadou, A. Maalej, A. B. Salah, A. Simon and M. Maglione, New relaxor ceramic with composition $BaTi_{1-x}(Zn_{1/3}Nb_{2/3})_xO_3$, *J. Alloys Compd.*, 2008, **452**(2), 451–455, DOI: 10.1016/j.jallcom.2007.03.056.

45 K. Uchino and S. Nomura, Critical Exponents Of The Dielectric Constants In Diffused- Phase-Trans Ition Crystals, *Ferroelectrics*, 1982, **44**(1), 55–61, DOI: 10.1080/00150198208260644.

46 I. Ouni, H. Ben Khlifa, R. M'nassri, M. M. Nofal, E. M. A. Dannoun, H. Rahmouni, K. Khirouni and A. Cheikhrouhou, Transport properties and dielectric response of $Pr_{0.8}Na_{0.2-x}K_xMnO_3$ ($x = 0$, 0.05, 0.1, 0.15 and 0.2) ceramics synthesized by sol–gel method, *Appl. Phys. A: Mater. Sci. Process.*, 2021, **127**(8), 12, DOI: 10.1007/s00339-021-04760-x.

47 X. Z. Zuo, J. Yang, B. Yuan, D. P. Song, X. W. Tang, K. J. Zhang, X. B. Zhu, W. H. Song, J. M. Dai and Y. P. Sun, Magnetic, dielectric properties, and scaling behaviors of Aurivillius compounds $Bi_{6-x/3}Fe_2Ti_{3-2x}(WCo)_xO_{18}$ ($0 \leq x \leq 0.15$), *J. Appl. Phys.*, 2015, **117**(11), 7, DOI: 10.1063/1.4915089.

48 M. B. Bechir and M. H. Dhaou, Study of Charge Transfer Mechanism and Dielectric Relaxation of $CsCuCl_3$ Perovskite Nanoparticles, *Mater. Res. Bull.*, 2021, **144**, 111473, DOI: 10.1016/j.materresbull.2021.111473.

49 P. Thongbai, S. Tangwancharoen, T. Yamwong and S. Maensiri, Dielectric relaxation and dielectric response mechanism in (Li, Ti)-doped NiO ceramics, *J. Condens. Matter Phys.*, 2008, **20**(39), 395227, DOI: 10.1088/0953-8984/20/39/395227.

50 M. Ram and S. Chakrabarti, Dielectric and modulus studies on $LiFe_{1/2}Co_{1/2}VO_4$, *J. Alloys Compd.*, 2008, **462**(1–2), 214–219, DOI: 10.1016/j.jallcom.2007.08.001.

51 K. Mencel, P. Durlak, M. Rok, R. Jakubas, J. Baran, W. Medycki, A. Ciżman and A. Piecha-Bisiorek, Widely used hardly known. An insight into electric and dynamic properties of formamidinium iodide, *RSC Adv.*, 2018, **8**(47), 26506–26516, DOI: 10.1039/c8ra03871f.